이학석사 학위논문

Suppression of charge density wave in $BaBiO_3$ thin films via controlling thickness and oxygen stoichiometry

$BaBiO_3$ 박막의 두께와 산소 화학당량 조절을 통한 전하 밀도파 억제연구

2016년 02월

서울대학교 대학원

물리천문학부

김 기 덕

Suppression of charge density wave in $BaBiO_3$ thin films via controlling thickness and oxygen stoichiometry

$BaBiO_3$ 박막의 두께와 산소 화학당량 조절을 통한 전하 밀도파 억제연구

지도 교수 노 태 원

이 논문을 이학석사 학위논문으로 제출함

2015년 12월

서울대학교 대학원

물리천문학부

김 기 덕

김기덕의 이학석사 학위논문을 인준함

2015년 12월

위 원 장 _____ (인)

부위원장 _____ (인)

위 원 _____ (인)

Preface

The charge disproportionated charge density wave (CDW) in $BaBiO_3$ is the periodical modulation of lattice and charge-density due to the valence skipping behavior in Bi ion. The insulating ground state and the pseudogap in the hole-doped bismuth oxide superconductors have been explained by this type of charge-density instability. Recently, in high T_c copper oxide superconductors, the presence of CDW in the ground state and competition between CDW and superconductivity attracted much attentions as a part of an effort to figure out the superconducting mechanism at high temperature. Also in bismuthate superconductors, it has been assumed that the pairing mechanism of the cooper pair is deeply related to the CDW ground state. Therefore, studying the nature of CDW in $BaBiO_3$ could be an excellent way to improve the understandings of high temperature superconductivity.

In this thesis, several parameters are tuned to manipulate the CDW, namely film thickness and oxygen stoichiometry, using pulsed laser deposition, spectroscopic ellipsometry, Raman spectroscopy, and x-ray diffraction. We found out that the charge-density instability is suppressed by reducing film thickness under critical thickness and generating oxygen vacancies. Furthermore, the oxygen vacancies are known to introduce extra electrons to the system, therefore the electronic structure of electron-doped $BaBiO_3$, which was predicted to be a topological insulator, is discussed with the help of optical spectrum.

Contents

Chapter 1

Introduction

1.1 Insulating mechanism of $BaBiO_3$

$BaBiO_3$ (BBO) is an insulating end member of high T_c superconductors ($Ba_{1-x}K_xBiO_3$ and $BaPb_{1-x}Bi_xO_3$) which is naïvely predicted to be a metal with $6s^1$ orbital configuration of Bi ion, however Bi^{4+} valence skipping due to relativistic contraction in Bi $6s^2$ electron pair [1] and consequent broken translational symmetry play a central role determining the electronic structure of this compound [2]. The skipped Bi^{4+} valences are substituted by alternatively ordered Bi^{3+} and Bi^{5+}, which is called charge-disproportionation, and this uneven charge distribution induces two types of distortion, octahedral breathing distortion and tilting distortion, leading to doubled unit cell.

The charge and lattice modulation in this material is called as charge disproportionated-charge density wave (CD-CDW), which has been adopted to explain the insulating and pseudo-gap properties of bismuthate superconductors. Especially, this CDW in BBO is distinguished from the other CDWs by two characters, one is the three dimensional nature which is rare property in solid-state physics, and the other is strong hybridization effect between bismuth and oxygen ion [3]. In this study, we tuned parameters to investigate those properties. In chapter 4, thickness is controlled to make use of the 3D nature of the CDW, and in chapter 5, concentration of oxygen vacancy is modulated to explore the effect of hybridization.

References

[1] A. W. Sleight, J. L. Gilson, and P. E. Bierstedt, *Solid State Commun*. **17**, 27 (1975).

[2] T. M. Rice and L. Sneddon, *Phys. Rev. Lett.* **47**, 689 (1981).

[3] K. Foyevtsova, A. Khazraie, I. Elfimov, and G.A. Sawatzky, *Phys. Rev. B* **91**, 121114 (2015).

Chapter 2

Backgrounds

2.1 Crystal structure of $BaBiO_3$

Barium bismuth oxide belongs to a structural class of material called perovskite that has composition ABO_3, where BO_6 octahedron not only acts as a basic structural building block, but also determines substantial portion of the electronic structure of the material. Therefore, in most cases B-O complex is subjected to closer investigation than A site atom. The most prominent examples are cuprate high T_c superconductors that are always called as 'cuprates' although they have various perovskite-based structures and complex compositions, because Cu-O_2 plane is the place where the superconductivity resides. Naturally, in BBO, BiO_6 octahedra are indispensable component in explaining its lattice and electronic structure.

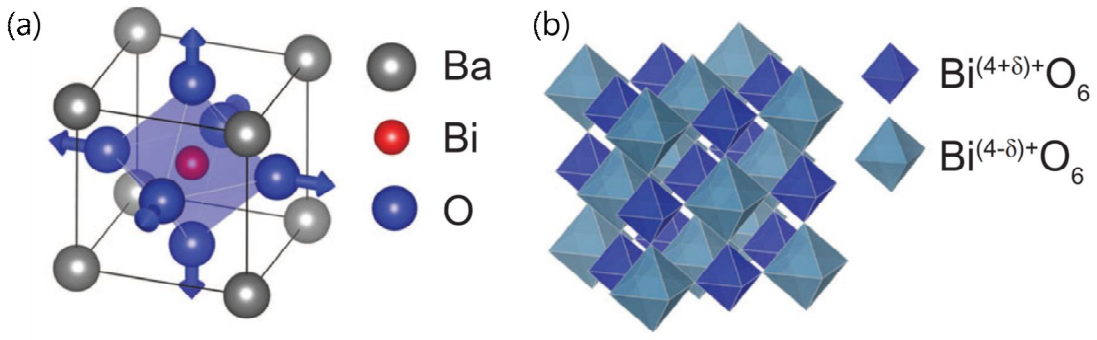

Figure 1. Lattice structure of $BaBiO_3$. (a) The pseudo-cubic unit of BBO, and the blue arrows correspond to the symmetric breathing phonon mode. (b) Checkerboard static breathing distortion in BBO. [2]

Pseudo-cubic unit cell of $BaBiO_3$ is depicted in Figure 1(a). At room temperature two classes of distortions reside in stoichiometric $BaBiO_3$; a breathing distortion and a tilting distortion. These lattice deformations are originated from the charge-density instability that segregates the valences of Bi into nominal Bi^{3+} and Bi^{5+}, and this fluctuating charge-density modulates the lattice periodically. Because a Bi ion with larger/smaller positive valence forms smaller/larger octahedron owing to larger/smaller Coulombic attraction, there exist two sizes of octahedra positioned nicely minimizing the Coulomb interaction. This type of distortion is called checkerboard breathing distortion, and is described in Figure 1(b). The breathing distortion is naturally followed by tilting distortion resulting in monoclinically distorted perovskite structure [1].

Apart from the monoclinic phase at room temperature, BBO has been known to exhibits various structural transitions depending on temperature and doping as in Figure 2(a), (b). For example, the stoichiometric BBO experiences monoclinic to rhombohedral, and rhombohedral to cubic transitions as temperature goes up. In the case of doped superconducting phase, the situation is still open to debate, however there was an interesting recent discovery that shows the coexistence of tetragonal and orthorhombic phase in stripe pattern [2].

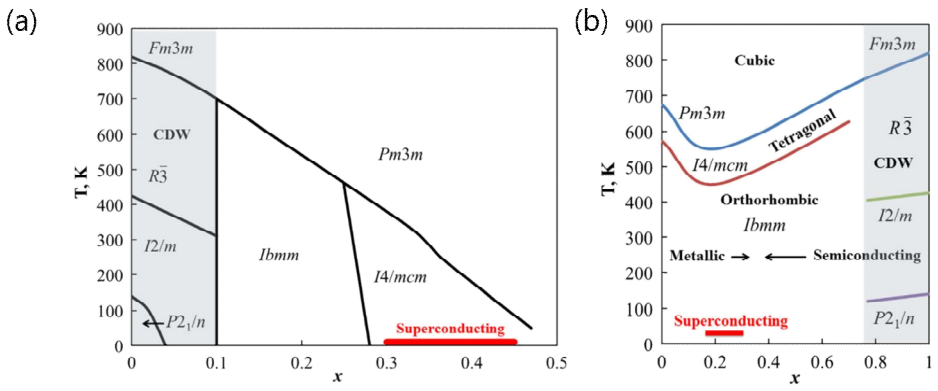

Figure 2. Phase diagrams of (a) BKBO and (b) BPBO. [3].

2.2 Studies on the lattice structure of $BaBiO_{3-x}$

In the view of perovskite oxide compound, oxygen vacancy is a type of point defect that can spoil the novel properties of oxides, for example high temperature superconductivity, quantum Hall effect could be damaged even by small amount of deviation from the ideal stoichiometry. However in some cases new phenomena are emergent from the oxygen vacancies such as bipolar superconductivity in cuprates [4], blue light emission in semiconducting titanates [5], and reversible brownmillerite-perovskite structural transition in cobaltates [6], mainly due to the fact that oxygen vacancies are able to act as electron donors in the system.

There were several reports on the effect of oxygen vacancies in $BaBiO_3$ focused on the anticipated metallic behavior in its electron-doped phase, whereas none of the results has shown any clue of insulator-to-metal transition adjusting oxygen vacancies. Thanks to these researches some information about the lattice structure of oxygen deficient BBO is available [7, 8], where phases with different portion of oxygen atoms are studied by means of x-ray diffraction and neutron scattering to construct a phase diagram as a function of oxygen content. The phase diagram displayed in Figure 3(a) contains three phases; structure of phase I and II is refined as cubic, but the structure of phase III is still in debate between layered structure presented in Figure 3(b) and non-layered tetragonal structure. In addition the CDW is known to survive only phase I, and vanish in phase II and III.

Recently, there was a seminal theoretical work that predicts a topologically insulating surface in electron-doped $BaBiO_3$, which means BBO is the first candidate for a topological insulator as an oxide. As an approach to the electron-doping, oxygen

vacancy is a more viable candidate than chemical doping, because chemical substitution in BBO has not been successful. Therefore, further studies on $BaBiO_{3-x}$ will be an exciting opportunity to explore the possibility of oxide topological insulator, and even to search the Majorana fermion in Josephson junction between oxide topological insulator and high T_c superconductor.

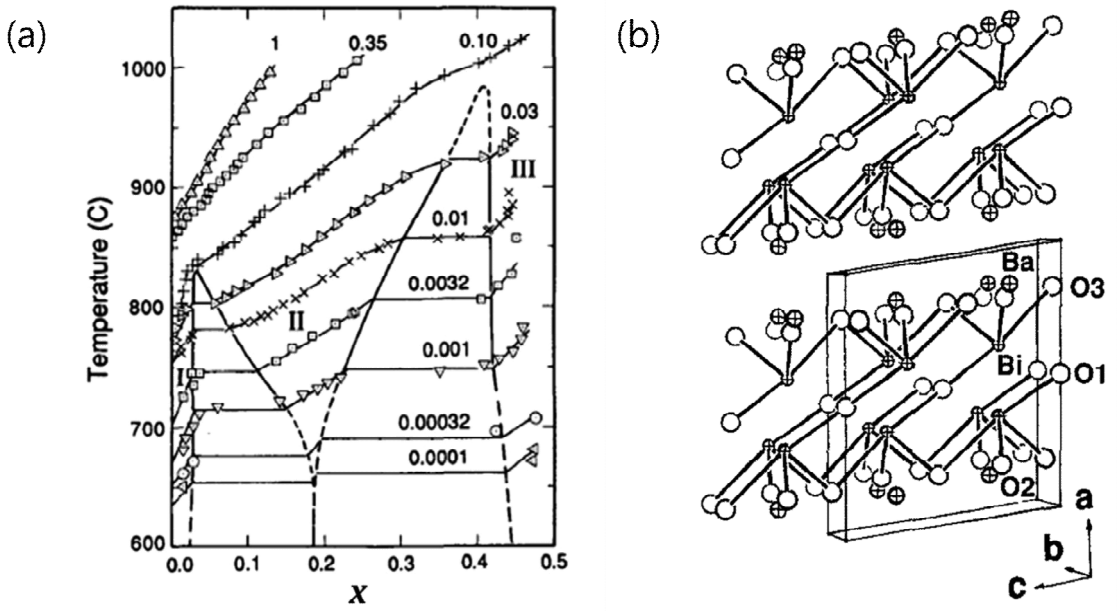

Figure 3. (a) The phase diagram of oxygen vacant $BaBiO_3$ [7]. (b) Layered structure of $BaBiO_{2.5}$. [9]

References

[1] P. V. Balachandran and J. M. Rondinelli, *phys. Rev. B.* **88**, 054101 (2013).

[2] P. Giraldo-Gallo, Y. Zhang, C. Parra, H. C. Manoharan, M. R. Beasley, T. H. Geballe, M. J. Kramer, and I. R. Fisher, *Nat. Commun.* **6**, 8231 (2015).

[3] A. W. Sleight, *Physica C* (Amsterdam) **514**, 152 (2015).

[4] Kouigi Segawa, M. Kofu, S-H. Lee, I. Tsukada, H. Hiraka, M. Fujita, S. Chang, K. Yanada and Yoichi Ando, *Nat. Phys* **6**, 579 (2010).

[5] Daisuke Kan, Takahito Terashima, Ryoko Kanda, Atsunobu Masno, Kazunori Tanaka, Shucheng Chu, Hirofumi Kan, Atsushi Ishizumi, Yoshihiko Kanemitsu, Yuichi Shimakawa and Mikio Takano, *Nat. Mat* **4**, 816 (2005).

[6] Hyoungjeen Jeen, Woo seok Choi, Michael D. Biegalski, Chad M. Folkman, I-Cheng Tung, Dilon D. Fong, John W. Freeland, Dongwon Shin, Hiromichi Ohta, Matthew F. Chisholm and Ho Nyung Lee, *Nat. Mat* **12**, 1057 (2013).

[7] R. A. Beyerlein, A. J. Jacobson and L. N. Yacullo, *Mat. Res. Bull* **20**, 877 (1985).

[8] Hiroshi Sakuma, Hiroo Hashizume and Atsushi Yamanaka, *Acta. Cryst* **B46**, 693 (1990).

[9] P. Lightfoot, J. A. Hriljac, Shiyou Pei, Ying Zheng, A. W. Mitchell, D. R. Richards, B. Dabrowski, J. D. Jorgensen and G. Hinks, *J. Solid. State. Chem* **92**, 473 (1991)

Chapter 3

Experimental Methods

3.1 Pulsed Laser Deposition

In studying solid-state physics, there are several parameters we can artificially tune, which include doping carriers, applying pressure, raising temperature, and so on. Tuning these parameters is essential in exploring various phase diagrams of solid-state materials where novel physical properties reside. We can add indispensable parameters, such as dimensionality, surface polarity, and strain, which we can utilize experimentally by making thin films [1, 2]. Especially for transition metal oxides, employing these variables is very useful to modulate the factors in Hubbard type models. Consequently, we can test theoretical models for novel physical phenomena like superconductivity, ferroelectricity, and topological phases with experimental methods.

Pulsed laser deposition (PLD) is one of the film fabrication techniques making use of high power excimer laser. This laser pulse is adopted to generate a plume of highly energetic plasma transferring ions from target material to surface of the substrate as depicted in Figure 1. This film growth process with ablation from pre-synthesized target gives large number of degrees of freedom for experimentalist, since stoichiometry could be easily calibrated. High temperature superconducting copper oxides are most famed members of materials, in which PLD is highly advantageous because of its complex stoichiometry [3].

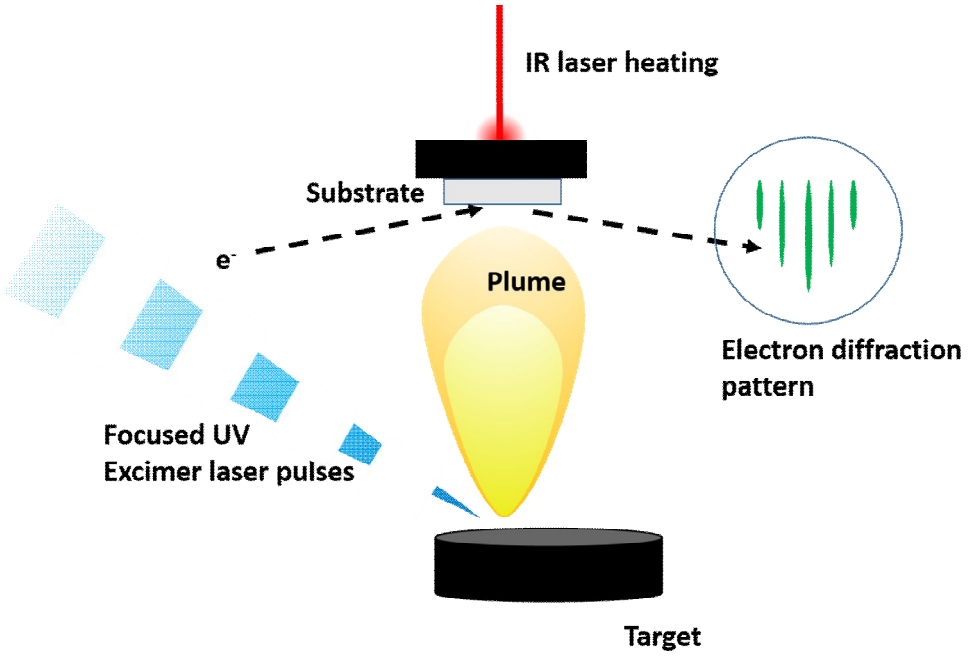

Figure 1. Schematic diagram of pulsed laser deposition. Whole deposition process is in UHV (~10^{-9} torr) chamber. Cylindrical target rotates around axis and travels back and forth during deposition to prevent repeated ablation at one spot. The SiC block dissipates heats from IR heating laser to substrate through platinum paste between the substrate and the block, and the temperature of the sample is tracked simultaneously with pyrometer. The electron diffraction image forms on the scintillating screen in a dark box, and recorded with a CCD camera.

In addition, diverse *in-situ* diagnostic methods are adopted to characterize films that are being grown in the deposition chamber. For instance, reflection high energy electron diffraction (RHEED), Spectroscopic ellipsometry (SE), and time-of-flight mass spectroscopy are able to obtain the information about surface quality, optical property, and composition of the plume.

The $BaBiO_3$ films analyzed in this work are grown by PLD with UHV system (Mobile Combie-Laser MBE system, Pascal. Co., Japan), excimer laser (LPXpro 210F, Coherent, USA), and pressed target (Toshima. Co., Japan). The base pressure of the deposition chamber is sustained below ~ 10^{-9} Torr with Turbo molecular pumps (TMP).

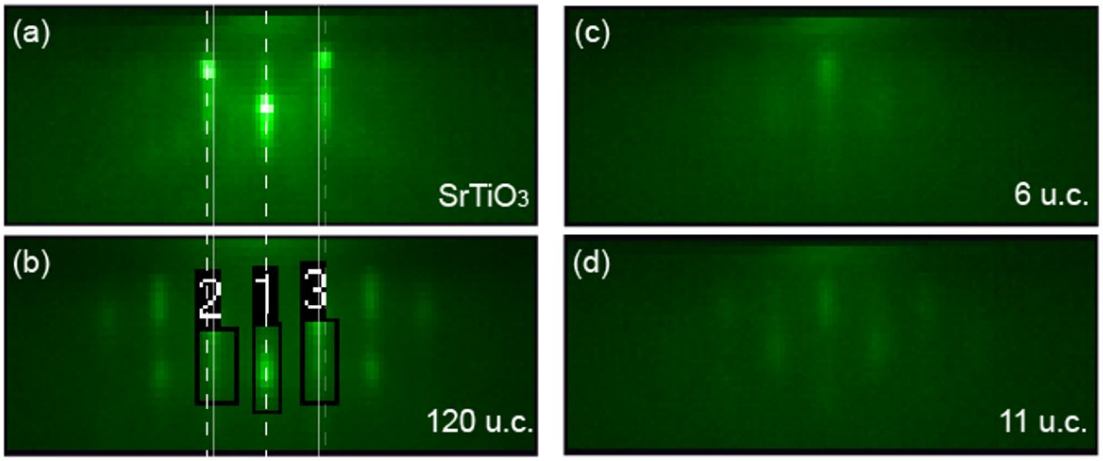

Figure 2. Reflection high energy electron diffraction pattern from $BaBiO_3$ thin films. (a) Clear RHEED pattern from $SrTiO_3$ substrate demonstrates high quality surface of the substrate. (b) 120 u.c. thick $BaBiO_3$ films have 3D growth mode, and shows smaller spacing between patterns than that of $SrTiO_3$. This means the in-plane lattice constant of the deposited film is larger than the substrate. (c) and (d) thin films also show sharp patterns.

This machine is equipped with load-lock chamber to prevent ultra-high vacuum chamber's repetitive exposure to air. Two different gases are able to be flowed inside using variable leakage valve, and the partial pressure of the gas is measured using capacitor diaphragm gauges and ion gauges. For in-situ characterization, high pressure (< 1 torr) RHEED gives information of surface structure of the film, and growth mode.

$BaBiO_3$ has considerably large lattice constant, $a_{pseudo\ cubic}$ = 0.4334 nm, compared to the other widely studied ternary oxide materials such as $SrTiO_3$ with $a_{pseudo\ cubic}$ = 0.3905 nm, which also is the most popular substrate for oxide thin films. Therefore, it is hard to find a commercial substrate that commensurate with $BaBiO_3$. Fortunately, there are several reports on PLD growth of $BaBiO_3$ thin film, in which they present well-grown $BaBiO_3$ films on $SrTiO_3$ substrates [4, 5]. We also could get high quality thin films on substrates with relatively large lattice mismatch, *viz*. $SrTiO_3$, $NdScO_3$

(a_{pc} = 0.4013 nm), $TbScO_3$ (a_{pc} = 0.3958 nm) , $SmScO_3$ (a_{pc} = 0.3987 nm), and MgO (a = 0.4212). Accordingly, range of mismatches ($a_{film} - a_{sub}/a_{sub}$) between substrate and film is from 8 % to 11 percent.

All the samples are grown under oxygen rich atmosphere with oxygen partial pressure $P_{O_2} = 100$ mTorr to avoid oxygen vacancy. During ablation, temperature of the substrate is kept at 500℃, and the energy density of the laser is calibrated to 0.6 J/cm^2. Deposited films are slowly cooled with 30℃/min to the room temperature in 100 mTorr oxygen atmosphere. Sample characterization is conducted with multiple methods, RHEED (Figure 2), x-ray diffraction (Figure 4), atomic force microscopy (Figure 6), and Rutherford backscattering, which demonstrate the high sample quality.

3.2 High Resolution X-ray Diffraction

Determination of electronic structure of all materials is one of the key goals in solid state physics. There are great deal of efforts to achieve this goal, which include both theoretical and experimental investigations, e.g., DFT, QMC simulations, and various spectroscopic techniques. However, one indispensable measurement one should conduct above all is the structural analysis of a given material, since the lattice structure governs the periodicity and symmetry of a system that are essential for resolving electronic structure. Major tools to get this information are scattering and microscopy, viz., x-ray diffraction, neutron scattering, and transition electron microscopy. Among above mentioned methods x-ray diffraction is the most popular one for the reasons that the commercial x-ray sources and diffractometers are available for an individual laboratory, that experimental procedure including sample preparation and measurement is uncomplicated, and that the results could be intuitively interpreted.

The principles of x-ray diffraction is based on the elastic scattering between electromagnetic wave and charged particles, in this case between x-ray and electrons, which is called Thomson scattering. Scattered waves from electrons in atoms interfere with each other constructively or destructively, and generate diffraction pattern due to the fact that the typical interatomic distance (~ 0.4 nm) is comparable with wavelengths of x-rays (e.g., Cu Kα ~ 0.154 nm and Mo Kα ~ 0.711 nm). The condition for diffraction maximum could be summarized as below equation (1).

$$2d_{hkl} \sin\theta = \lambda \qquad (1)$$

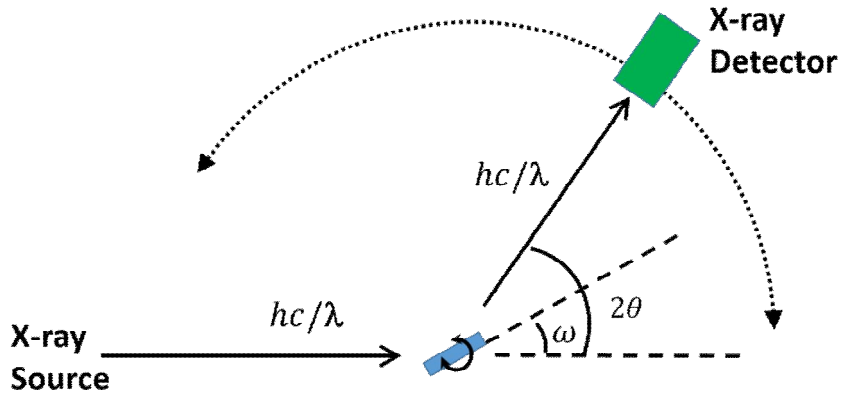

Figure 3. X-ray diffraction experimental configuration. X-ray source is fixed in this setup, instead detector and sample stage rotate around the center. 2θ is the angle between incident x-ray and detector, and ω is the sample rotation angle.

Where d_{hkl} is an interplanar spacing between atomic planes, which could be expressed in pseudo-cubic notation ($(h^2 + k^2 + l^2)/a_{pc}{}^2$), λ is the wavelength of the incident x-ray, and θ is as described in the figure 3. Now, one can calculate the lattice parameters based on this equation using positions of diffraction maxima.

Typical measurement trick is called 2θ–ω scan, in which detector and sample rotate coherently to scan along parallel planes. Figure 4 (a) shows an example of 2θ–ω scan

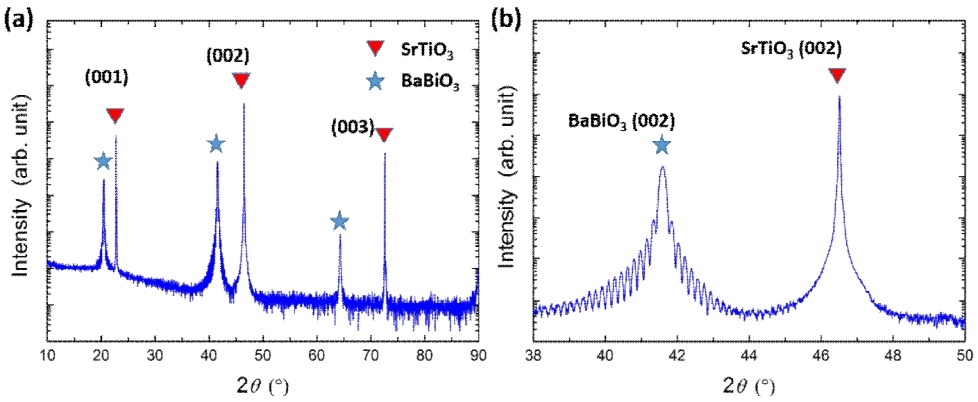

Figure 4. 2θ–ω scan of 92 unit cell (u.c.) thick $BaBiO_3$ film on $SrTiO_3$ substrate. Peaks with blue stars are assigned as reflections from $BaBiO_3$, and peaks with red wedges are from $SrTiO_3$.

along (00l) planes. This scan manifests that the crystal orientation of $BaBiO_3$ thin film is well aligned with that of $SrTiO_3$, and that the other phases are absent. In addition to the crystal orientation and phase determination, one can also get information about film thickness by closely surveying the 2θ–ω scan. In Figure 4 (b), a number of periodic oscillations are around the (002) reflection of $BaBiO_3$ peak. This oscillation is originated from the thin-film interference, and the relation between period of this oscillation (ΔQ) and film thickness (t) follows the equation below.

$$t = \frac{2\pi}{\Delta Q}, \text{where } Q = 4\pi\frac{sin\theta}{\lambda} \quad (2)$$

In this work, film deposition rate is determined by above relation, and crosschecked with RHEED oscillation and stylus profiler.

Structural refinements based on x-ray diffraction were conducted at home laboratory with D8 Discover diffractometer using Cu Kα source (Bruker Co., Germany), and at Pohang Accelerator Laboratory 3A beamline that is equipped with six circle diffractometer. This results will be discussed in chapter 4 and 5.

3.3 Spectroscopic Ellipsometry

Optical investigations of the samples are widely used for determining the electronic properties of various materials including transition-metal oxides, organic conductors, and Si based semiconductors. Spectroscopic ellipsometry is a type of optical spectroscopy utilizing the fact that reflected light from a sample surface becomes elliptically polarized. From the elliptically polarized light two parameters are obtained, namely amplitude ratio ψ and phase difference Δ between s- and p- polarized light. Based on these two parameters, optical constants such as $\tilde{\varepsilon}, \tilde{\sigma}$ could be directly acquired without Kramers-Kronig relation which is essential in some optical spectroscopies measuring transmittance or reflectance.

In this study, optical spectroscopy is carried out using two types of ellipsometers, one is V-VASE (J.A. Woolam Co., USA) for high accuracy measurement on ultra-thin films, and the other one is M-2000D (J.A. Woolam Co., USA) for real-time measurement on samples in the UHV PLD chamber. The experimental configuration of the real-time measurement is depicted in Figure 5.

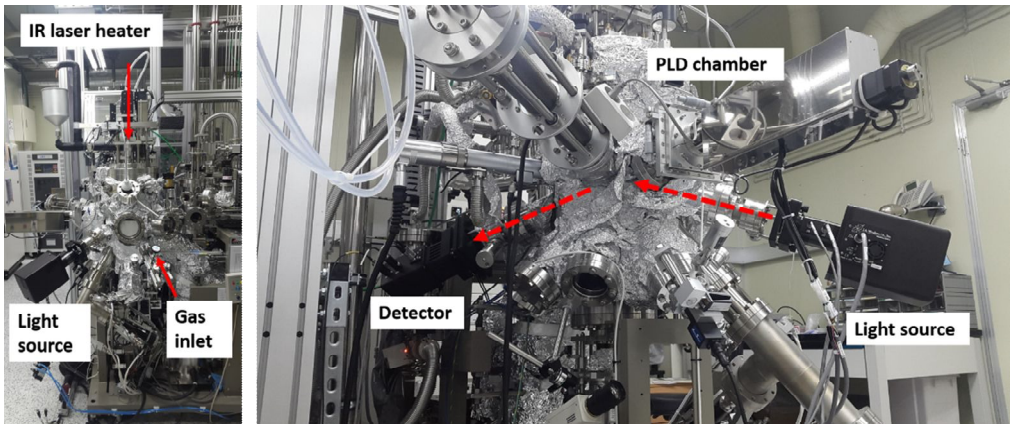

Figure 5. Experimental setup for real-time spectroscopic ellipsometry, which is equipped with IR laser heater, ion gauge, variable leakage valve, and M-2000D ellipsometer.

3.4 Atomic Force Microscopy

Atomic force microscopy is performed to investigate the surface morphology of the PLD grown samples on an Asylum Instrument Cypher atomic force microscope (AFM) using cantilevers with a spring constant of ~ 40 N/m. Surface topographic data is collected employing non-contact mode AFM, and the data is processed with Gwyddion software package. Figure 6 contains dataset representing thick (> 100 u.c.) films that are studied in this study. These images show clear step and terrace features, with roughness $R_a \cong 0.8 - 2.6$ Å, which indicates highly flat surface even in thick films.

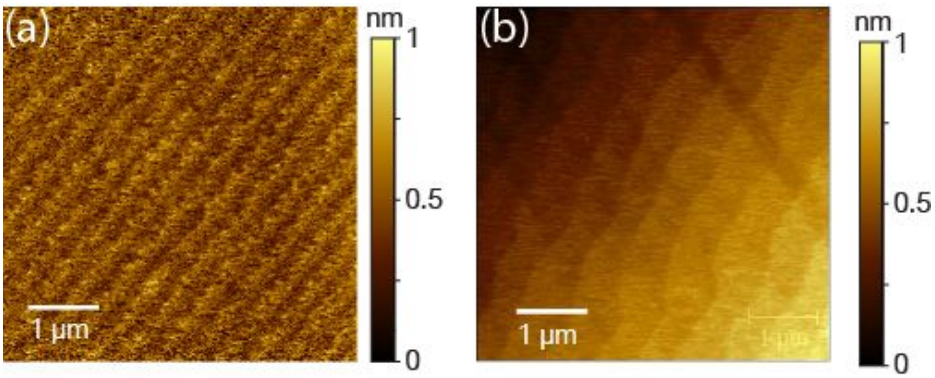

Figure 6. AFM images of (a) 100 unit cells thick BBO on STO, and (b) 100 unit cells thick BBO on NSO.

3.5 Raman Spectroscopy

Raman spectra are acquired on a Renishaw inVia Raman microscope for excitation wavelength 514.5 and 632.8 nm with a 50x objective. Illumination power is calibrated to be less than 1 mW on laser spot size ≅ 1 μm, with 10 seconds integration time, to prevent unintended sample heating with laser. To extract the Raman signal from ultra-thin films, the focus of the laser is tuned to be right on the sample surface.

References

[1] H. Y. Hwang, Y. Iwasa, M. Kawasaki, B. Keimer, N. Nagaosa and Y. Tokura, *Nat. Mat* **11**, 103 (2012).

[2] P. D. C. King, H. I. Wei, Y. F. Nie, M. Uchida, C. Adamo, S. Zhu, X. He, I. Božović, D. G. Schlom and K. M. Shen, *Nat. Nanotech* **9**, 443 (2014).

[3] P. R. Willmott and J. R. Huber, *Rev. Mod. Phys* **72**, 315 (2000).

[4] Kei Inumaru, Hajime Miyata and Shoji Yamanaka, *Phys. Rev. B* **78**, 132507 (2008).

[5] A. Gozar, G. Logvenov, V. Y. Butko and I. Božović, *Phys. Rev. B* **75**, 201402(R) (2007).

Chapter 4

Suppression of Three Dimensional Charge Density Wave via Dimensional Control in $BaBiO_3$ Thin Films

Three dimensional charge density wave is strongly related to the emergence of high T_c superconductivity in the bismuth based compounds ($Ba_{1-x}K_xBiO_3$, $BaPb_{1-x}Bi_xO_3$, etc.) [1], therefore the suppression of charge density wave (CDW) is worth studying carefully. On the other hand, it is complicated to study chemically doped material, because chemical doping introduces multiple effects including carrier introduction, point defect, and chemical pressure, etc. In this study, thickness dependence of CDW in the mother compound, stoichiometric $BaBiO_3$ thin film, is studied ruling out the effect of chemical pressure and point defect.

4.1 Observation of structural transition by HR-XRD

In this section, I evaluate the lattice structures of the undoped $BaBiO_3$ thin films with different thicknesses using high resolution XRD. Figure 1(a) displays the diffraction maxima from $BaBiO_3$ and $SrTiO_3$ (002) reflections in 2θ–ω scan demonstrating that the c-axis of pseudo-cubic $BaBiO_3$ is well-oriented along that of $SrTiO_3$ substrate. Interference oscillations in the graphs confirm that surface of the films and the substrate interface are smooth, and could be used to calculate the thickness of the film using the equation (2). Pseudocubic c-lattice parameter of thick $BaBiO_3$ film is computed as 4.334 ± 0.008 Å from the peak position of the diffraction

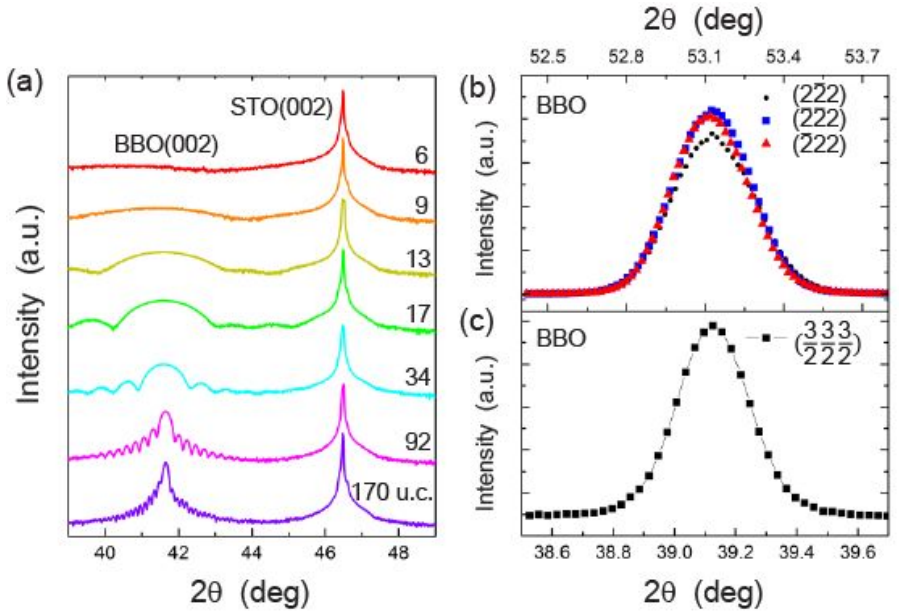

Figure 1. Results of high resolution x-ray diffraction. (a) 2θ–ω scan around BBO (002) and STO (002), and the numbers on the right side of the plot are thicknesses in the unit of unit cells., (b) 2θ–θ scan of $(\bar{2}22)$, $(2\bar{2}2)$ and $(22\bar{2})$ reflections, (c) 2θ–ω scan of $(\frac{3}{2}\frac{3}{2}\frac{3}{2})$ reflection. [2]

maximum, which is consistent with the values that are reported previously using bulk samples [3]. Further structural refinement was done utilizing synchrotron x-ray source, and the results are presented in Figure 1(b) and 1(c). Figure 1(b) displays 2θ–ω scans at different phi values showing $(\bar{2}22)$, $(2\bar{2}2)$ and $(22\bar{2})$ reflections which have identical values of reflection maxima positions. This proves that the $BaBiO_3$ has tetragonal structure in thick films. This result is consistent with the previous work which reported the tetragonal structure of $BaBiO_3$ thick films [4]. The breathing distortion associated with CDW could be detected as XRD peaks with half-integer reflections due to the fact that the unit cell is doubled by static breathing distortion. Figure 1(c) corresponds to the $(\frac{3}{2}\frac{3}{2}\frac{3}{2})$ reflection's diffraction maximum in the 2θ–ω scan, therefore it is evident that static breathing distortion is present in the thick $BaBiO_3$ film, which is consistent with the results of previous study.

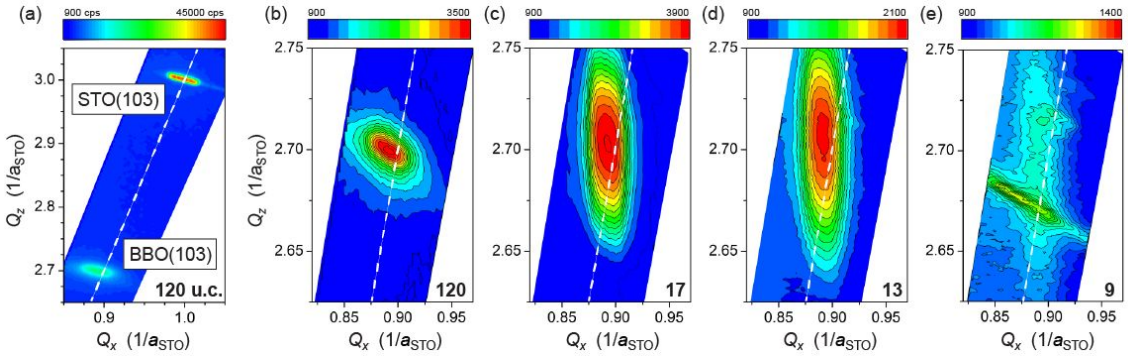

Figure 2. Reciprocal space mappings around BBO (103) and STO (103) reflections. White dashed lines in the graphs correspond to the positions that are supposed to have cubic symmetry [2].

In addition to the 2θ–ω scans above, XRD reciprocal space mappings (RSM) in the vicinity of STO (103) were carried out to investigate possible structural changes in the $BaBiO_3$ thin films as a function of film thickness. Figure 3 shows the RSM scans that were collected from the BBO films using lab source x-ray diffractometer. Since these scans are spanned into both Q_x and Q_z, the evolutions of in-plane and out-of-plane lattice constants could be simultaneously inspected. According to Figure 3(a) the film is fully relaxed in view of the fact that the Q_x position of the BBO (103) is far different from that of STO (103) in reciprocal space. Moreover, finite distance from white dashed line to (Q_x, Q_z) of BBO (103) peak means that the lattice structure of 120 u.c. thick BBO is deviated from cubic structure. Same deviation is observed in 17, 13 u.c. thick films shown in Figure 3(c), 3(d). By contrast, as shown in Figure 3(e), a peak from BBO (103) reflection is shifted toward lower value of Q_z for 9 u.c. film, indicating an abrupt 1% increase in the c-axis parameter. One remarkable point is that this new position of diffraction maximum is located right on the white dashed line, which suggests a structural phase transition from tetragonal to cubic occur between 13 and 9 unit cells.

4.2 Change in lattice symmetry measured by Raman spectroscopy

In the previous section, tetragonal to cubic transition is suggested based on high resolution x-ray diffraction data. To confirm this transition, more concrete experimental evidences are needed, which is sensitive to lattice symmetries. Raman spectroscopy provides firm evidence about lattice distortions in $BaBiO_3$. The symmetry of oxygen breathing phonon mode that mediates the coupling between the lattice and electronic properties of BBO belongs to a group A_g, and distortions such as tilting, or static breathing distortion make this mode Raman-active. On the other hand, the breathing phonon mode should be Raman-inactive, if there is no deviation from the ideal cubic perovskite structure. According to the previous study done by Tajima *et al.*, Raman spectra of BBO showed a dominant maximum at $\approx$ 565 cm^{-1} that corresponds to first-order breathing phonon mode, and the intensity of this peak is at a maximum for an illumination with $\lambda = 633$ nm (~ 1.96 eV) due to the resonance with the direct band gap of BBO (~ 2 eV). This peak was gradually attenuated via increasing doping concentration and totally suppressed at $x \cong 0.4$, where a structural transition from monoclinic to a cubic $Pm\bar{3}m$ lattice structure occurs [5].

Raman spectra of the stoichiometric BBO films on STO that were grown with PLD are displayed in Figure 4, which shows a clear thickness-dependent evolution. In the spectrum of the 130 u.c.-thick BBO film, the prominent peak feature correlated with breathing phonon mode is shown in the Figure 4(a). As the film thickness decreased, the intensity of this characteristic peak also reduced systematically, however this peak

unexpectedly vanished totally in films thinner than 13 unit cells. In the magnified plot (see Figure 4(b)), Raman spectra of films thinner than 13 u.c. are indistinguishable from that of STO. As shown in Figure 4(c), the same behavior is observed by the Raman spectroscopy with a different illumination wavelength (λ = 514 nm), in which the first-order breathing phonon mode peak is intrinsically smaller as a result of the off-resonance with band gap. Peak intensities are plotted as a function of film thickness in Figure 4(d) in order to figure out the critical thickness of the complete suppression of the peak from the breathing phonon mode. As evident from the figure, the critical thickness, where breathing phonon mode in BBO becomes Raman in-active, is inferred to be 11 ± 2 u.c.. Consequently it is more evident that BBO underwent a structural transition from tetragonal to cubic eliminating the structural distortions by reducing film thickness.

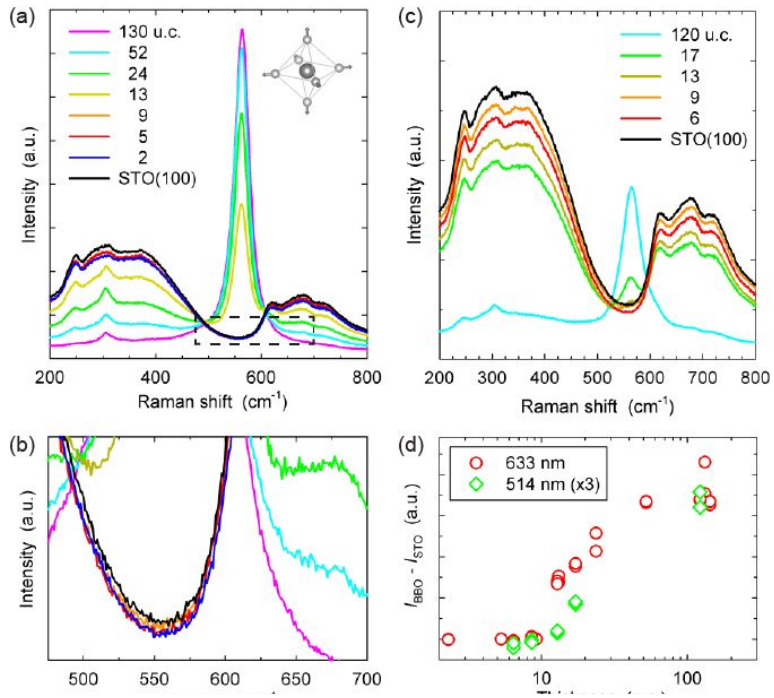

Figure 3. [2]. Raman spectroscopic characterization of the BBO films. (a) The Raman response at λ= 633 nm. (b) Magnified view of the Raman spectra. (c) The Raman response at λ= 514 nm. (d) evolution of the intensity of the Raman spectrum at ~ 565 cm^{-1}.

4.3 Suppression of CDW gap population via thickness control

The long-range CDW in BBO not only accompanies structural breathing distortion also forms a Peierls gap at the Fermi level because of the doubled lattice periodicity. This gap has been observed as a prominent maximum in the optical conductivity $\sigma_1(\omega)$ at around 2 eV, and has been explained by the presence of CDW ordering. To track the evolution of charge ordering as a function of the sample thickness, optical conductivity is measured for BBO films via spectroscopic ellipsometry. As shown in Figure 4(a), we observed a strong peak at $\cong$2 eV in the spectrum of the 92 u.c. thick BBO films. As we decreased the thickness to 34, 17, and 13 u.c., the amplitude of this peak in $\sigma_1(\omega)$ gradually decreased. Further thickness reduction led to a strong suppression of this peak, leaving only an indistinct and broad feature in $\sigma(\omega)$ for 9 u.c. thick BBO and 6 u.c. thick BBO, which is indicative of a melting of CDW order. The thickness dependence of $\sigma_1(\omega)$ at 2 eV shown in Figure 4(b) suggests that this melting of charge order occurs as a sudden transition at a critical thickness in the range 9-13

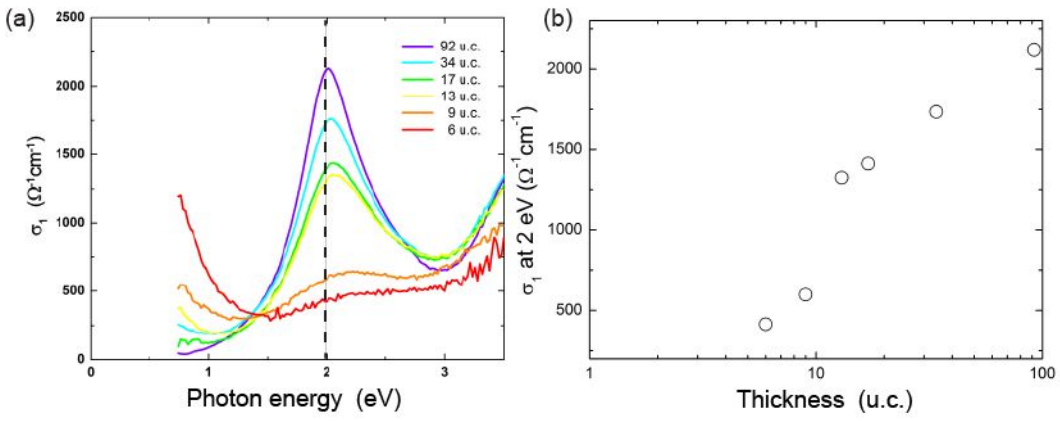

Figure 4. (a)Optical conductivity of the BBO thin films. (b) Optical response at 2 eV.

u.c., which coincides with the structural transition to a cubic $Pm\bar{3}m$ lattice evidenced by the disappearance of the Raman activity of the oxygen breathing phonon mode, as shown in Figure 3(d).

Varying the thickness provides a means to control CDW ordering in BBO without the complexities associated with extrinsic doping. In bulk BKBO, increasing the doping density x leads to a progressive reduction in the optical band gap energy to below 2 eV and to the appearance of an additional peak at around 0.85 eV due to the formation of bipolarons (see, for example, Fig 1 in Ref. [6]). Neither effect is visible in the spectra acquired for the BBO films, for which the absorption maximum remained at 2 eV regardless of the film thickness. This important difference highlight the distinct advantage of thickness control, which avoids the introduction of additional charge carriers or disorder into BBO films.

4.4 Discussion

Taken together, our XRD, ellipsometry, and Raman spectroscopy observations provide considerable insight into the effects of thickness on the BBO films. For films thicker than critical thickness, $d_c \cong 11$ u.c., the films exhibit a structural distortion due to tilting of the BiO_6 oxtahedra, as well as static breathing distortion that comprises two nonequivalent Bi sites and a concomitant CDW, analogous to the case of bulk BBO. With films thinner than critical thickness, however, the tilting and breathing distortions abruptly disappear, accompanied by suppression of the CDW. We conclude that $d_c = (11 \pm 2)$ u.c. represents a critical length scale for the stability of the 3D checkerboard CDW pattern in BBO. Intriguingly, the length scale observed in our study is comparable to the typical grain size of the tetragonal polymorph found in BPBO single crystals, as well as to the superconducting coherence length at optimal doping [7], which suggests that real-space and momentum-space pairing in the bismuthates share a common characteristic length scale.

Previous experimental and theoretical work has consistently shown that, in the absence of lattice distortions, the cubic $Pm\bar{3}m$ phases of bismuthates are metallic [8-10]. This suggests that the sudden disappearance of lattice distortions in BBO thin films at $d_c = 11$ u.c. may be accompanied by an insulator-to-metal transition. This accords with the observation that in the optical conductivity spectra shown in Figure 4(a), concurrently with the suppression of the peak at 2 eV, a Drude-like peak appears at energies below ~ 1 eV; this transfer of spectral weight in $\sigma_1(\omega)$ may signal an incipient thickness-controlled insulator-to-metal transition, analogous to the behavior observed in bulk BPBO and BKBO. In electrical transport measurements, thick BBO

films are insulating, as expected. However, so far no reliable measurements have been obtained for $d < d_c$. This may be due to contact-induced oxygen depletion; however, an alternative, speculative scenario is suggested by the observation that at $d < d_c$, the peak in $\sigma_1(\omega)$ at 2 eV is not completely suppressed. While the oxygen breathing phonon mode is Raman inactive in the undistorted $Pm\bar{3}m$ lattice, it might still provide sufficient coupling to stabilize residual CDW order in this thickness regime, which may compete with the incipient metallic state. Further measurements are in progress to clarify this phenomenon.

References

[1] A. W. Sleight, *Physica C* (Amsterdam) **514**, 152 (2015).

[2] Gideok Kim, Michael Neumann, Minu Kim, Manh Duc Le, Tae Dong Kang and Tae Won Noh, *phys. Rev. Lett.* **115**, 226402 (2015).

[3] D. G. Hinks, B. Daborowski, J. D. Jorgensen, A. W. Mitchell, D. R. Richards, Shiyou Pei and Donglu Shi, *Nature* **333**, 836 (1988).

[4] Kei Inumaru, Hajime Miyata and Shoji Yamanaka, *Phys. Rev. B* **78**, 132507 (2008).

[5] S. Tajima, M. Yoshida, N. Koshizuka, H. Sato, and S. Uchida, *Phys. Rev. B* **46**, 1232 (1992).

[6] T. Nishio, J. Ahmad, and H. Uwe, *Phys. Rev. Lett.* **95**, 176403 (2005).

[7] P. Giraldo-Gallo, Y. Zhang, C. Parra, H. C. Manoharan, M. R. Beasley, T. H. Geballe, M. J. Kramer, and I. R. Fisher, *Nat. Commun.* **6**, 8231 (2015).

Chapter 5

Temperature, Oxygen vacancy & CDW in $BaBiO_3$ thin films

In metal oxide compounds, it is impossible to exaggerate the importance of oxygen. Oxygen ions mediates hoping of an electron, construct oxygen cages that determine symmetries of crystal, and of course take electrons from metal. Naturally, oxygen vacancy (V_O) should be crucial for properties of metal oxides. Especially, it was reported that the symmetry of oxygen octahedral plays major role in the hybridization of Bi-O bonding and charge density wave [1], therefore one can expect that oxygen vacancies have considerable effect in the electronic and lattice structure of $BaBiO_3$. In this study the effects of oxygen vacancy are investigated extensively with HR-XRD, real-time spectroscopic ellipsometry in $BaBiO_3$ thin films. The films subjected to all measurements in this study are all grown on $NdScO_3$ substrate, because of its robustness at high temperature and relatively plain optical absorption spectrum in the energy range in which CDW gap locates.

5.1 Reversible formation of oxygen vacancies accompanying suppression of charge density wave

In this section, formation of oxygen vacancy as functions of annealing time and temperature is studied by real-time spectroscopic ellipsometry. For the purpose of

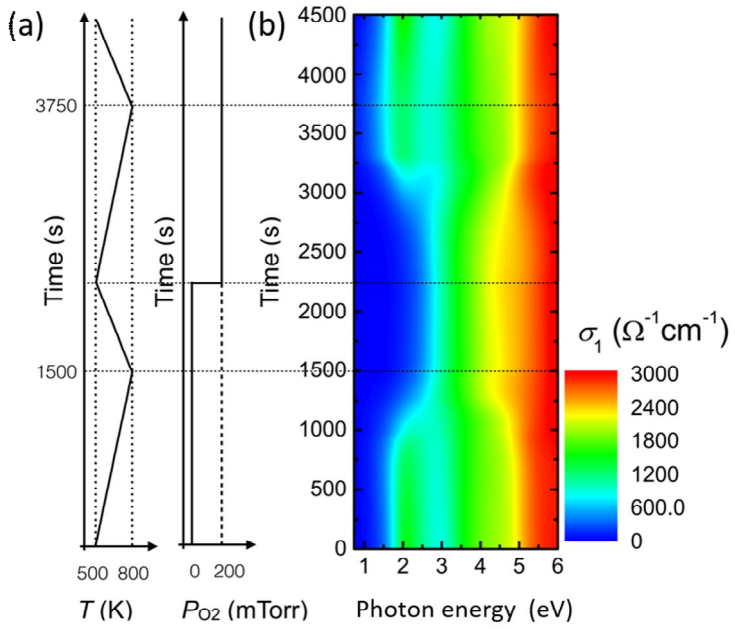

Figure 1. Results of real-time ellipsometry. (a) experimental condition including oxygen partial pressure and annealing temperature. (b) Contour plot of σ_1 (ω) as a function of annealing time.

getting oxygen atoms out of the compound, high temperature annealing was carried out under high vacuum. In order to determine the critical temperature from which oxygen vacancies form, a thin film sample (d ~ 43 nm) was heated and cooled with condition given in Figure 1(a). This annealing procedure could be categorized into two cycles, one is V_O-generating (vacuum-anneal) cycle and the other is oxygen-refilling (high pressure oxygen anneal) cycle.

Contour plot in Figure 1(b) displays the real part of the optical conductivity, σ_1 (ω), as a function of temperature and time, where the characteristic optical absorption maximum at ~ 2 eV associated with CDW is clearly present initially. In the first cycle, as temperature went up this absorption peak became smaller, and abruptly vanished at t ≅ 1200s. Based on the fact that this peak did not recovered in cooling ($1500 < t < 2250$), this complete suppression of peak is not a simple temperature dependent phenomenon. In the second cycle under high pressure of oxygen, the peak

at 2 eV appeared at t≅3000s, and remained after cooling. This observation of reversible phase transition is consistent with previous reports by Beyerlein *et al* [2]., which presented a phase diagram of $Ba_2Bi_2O_{6-x}$ that consist of three phases, viz. phase I ($0 < x < 0.05$), phase II ($x \approx 0.2$), and phase III ($0.4 < x < 0.5$). Using powder x-ray scattering they claimed that CDW order can survive the phase I, but not phase II and III. Consequently, we suggest that the suppression of an optical gap from CDW, which accompanies the phase transition from phase I to phase II, be observed by real-time optical spectroscopy for the first time, and this transition was able to be straightforwardly reversed by high pressure oxygen annealing.

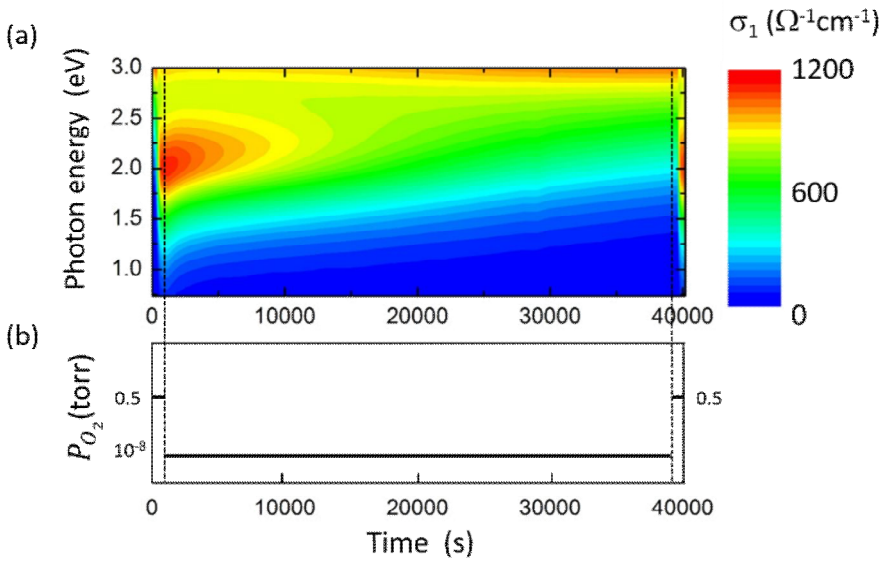

Figure 2. Result of real-time spectroscopic ellipsometry at fixed temperature. (a) Contour plot of σ_1 (ω) as a function of annealing time. (b) Experimental condition including oxygen partial pressure as a function of annealing time.

To compare oxygen gaining and loosing process, another measurement was conducted with temperature fixed at 673 K (400 ℃), and oxygen partial pressure controlled. The evolution of optical conductivity is displayed in Figure 2(a), where a

maximum at 2 eV developed very sharply and decayed gradually as oxygen is introduced and removed. It is clearly demonstrated that the CDW in BBO can easily controlled by generating and refilling oxygen vacancies.

5.2 Vacuum-annealing x-ray scattering study on the charge density wave in $BaBiO_3$ thin films

In the previous section, the experiments were focused on the dynamical reversibility of the oxygen in-and-out process. For fundamental interests it would be intriguing to study the temperature dependence of the CDW carefully, since the unexpected insulating and superconducting mechanism is known to be closely related with the CDW in BBO. We used two methods to explore behaviors of CDW, one is XRD-based structural analysis that can pick the signal from the characteristic periodicity of CDW, and the other is optical spectroscopy in which we are utilizing the 2 eV absorption maximum known to be associated with long-range CDW order [3]. In this section, structural phase transition from phase I to phase II, and suppression of a diffraction maximum from commensurate CDW are to be discussed with help of XRD datasets.

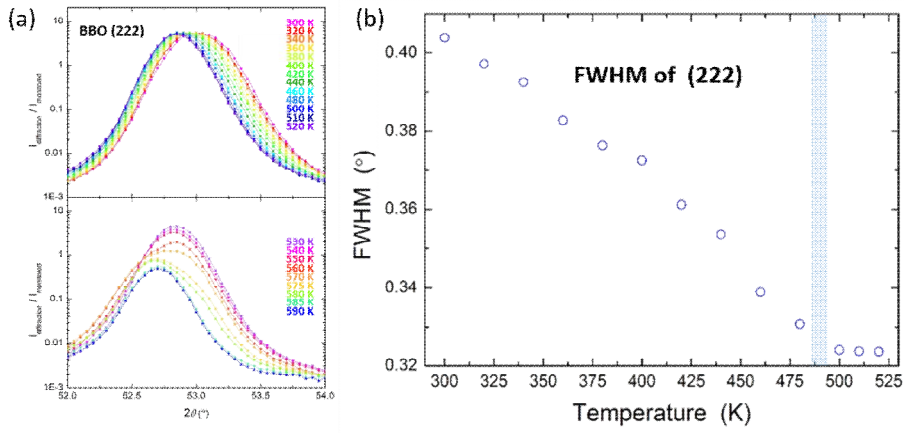

Figure 3. HR-XRD data obtained using a synchrotron light source. (a) BBO (222) reflections. (b) Full width at half-maximum of BBO (222) peaks.

The BBO (222) reflections shown in Figure 3(a) are subject to analysis, because this reflection has high intensity and is in the same plane with $(\frac{3}{2}\frac{3}{2}\frac{3}{2})$ peak that will be utilize to investigate the behavior of CDW. For the vacuum annealing condition, the sample stayed at measurement temperature for ~ 60 min before acquiring data such that the sample can reach a pseudo-equilibrium state. The temperature dependence of (222) peak could be classified into two groups, one is lower temperature region $(300\mathrm{K} < \mathrm{T} < 520\mathrm{K})$ accompanied by simple peak shift without major change in peak shape, the other is higher temperature region $(520\mathrm{K} < \mathrm{T} < 590\mathrm{K})$ showing development of new feature. Figure 3(a) summarizes lower temperature behavior in the upper panel and higher temperature behavior in the lower panel. The noticeable features appeared at higher temperatures; the peak was broadened initially, and separated into two peaks. The original peak became smaller and totally suppressed, while the new peak at lower angle became dominant. This situation is explained by transition from stoichiometric phase I (tetragonal, a=b=0.4379 nm and c=0.4333 nm) to oxygen-deficient phase II (tetragonal a=b=0.4394 nm and c=0.4364 nm) with larger lattice parameters. In order to assign the critical behavior of this phase transition, in Figure 3(b) the temperature dependence of the FWHM is studied at temperatures incipient with the boundary between lower and higher temperature regime. A sharp alteration from monotonic decrease to constant is observed at ~ 480 K, which can be assigned as critical temperature of a phase transition.

To probe the changes in CDW, we analyzed a half integer $(\frac{3}{2}\frac{3}{2}\frac{3}{2})$ reflection that is displayed in Figure 4(a). It is evident that the peak is getting smaller as the sample is being heated up. By Gaussian fitting we could get the intensities of the peaks as a

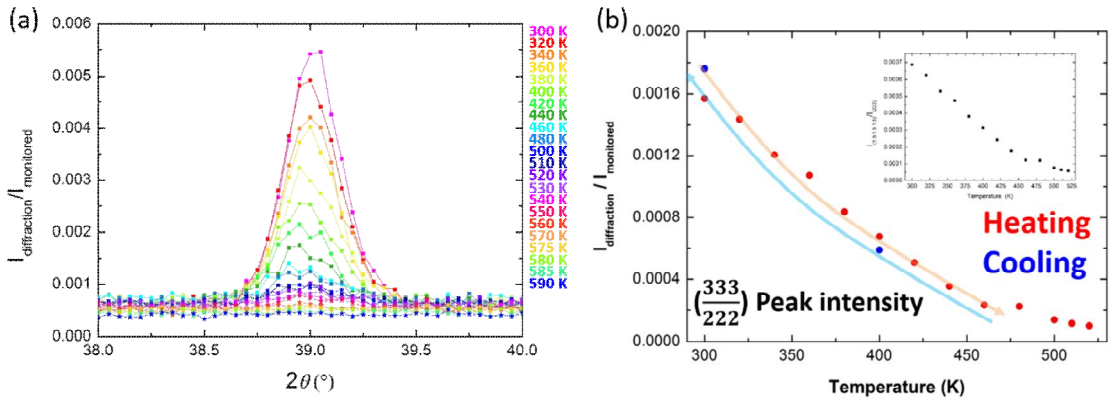

Figure 4. . HR-XRD data obtained using a synchrotron light source. (a) BBO $(\frac{3}{2}\frac{3}{2}\frac{3}{2})$ reflections. (b) Temperature dependence of the intensity of BBO $(\frac{3}{2}\frac{3}{2}\frac{3}{2})$ reflection.

function of temperature, which is plotted in Figure 4(b). At temperatures between 300K and 480K the peak intensity monotonically decreases, moreover it is recovered totally by cooling down suggesting that softening of lattice doubling in this temperature range is not from the formation of oxygen vacancies in the film. In contrast, cooling down after heating up to over 480K didn't revive the lattice doubling. To separate the pure behavior of CDW from the thermal broadening of the peak, the inset of Figure 4(b) gives the plot of diffraction intensity divided by (222) peak intensity, which is almost indistinguishable from the undivided intensity plot. It is remarkable that limiting temperature of half-integer reflections is consistent with the critical temperature from the (222) reflection measurement.

5.3 Vacuum-annealing real-time ellipsometry study on the charge density wave in $BaBiO_3$ thin films

The evolution of optical spectra as a function of temperature is elaborated in this section. Like in the previous section, samples are kept at one temperature for ~ 60 min before acquiring spectrum. Figure 5(a) displays the real part of optical conductivities, σ_1, at different temperatures, where two notable changes are observed, one is the suppression of the peak at 2 eV corresponding to the gap induced by CDW ordering and the other is the enhancement of the spectral weight at higher energy ($3\ \text{eV} < E < 5\ \text{eV}$). For further investigation of 2 eV peak, a magnified view around the 2 eV peak is plotted in figure 5(b). Apart from the reduced peak intensity upon heating, the evolution of peak position experience anomaly at particular temperature, which is guided by dashed arrows in the figure; initially the peak moves to lower energy on the other hand, at higher temperature the direction is changed toward higher energy. In order to track the trend of peak position more precisely, peak positions are estimated using Lorentz-Gaussian fitting, and the results are summarised in the inset to the Figure 5(b) demonstrating that the sign of the gradient dramatically flipped at around 450K.

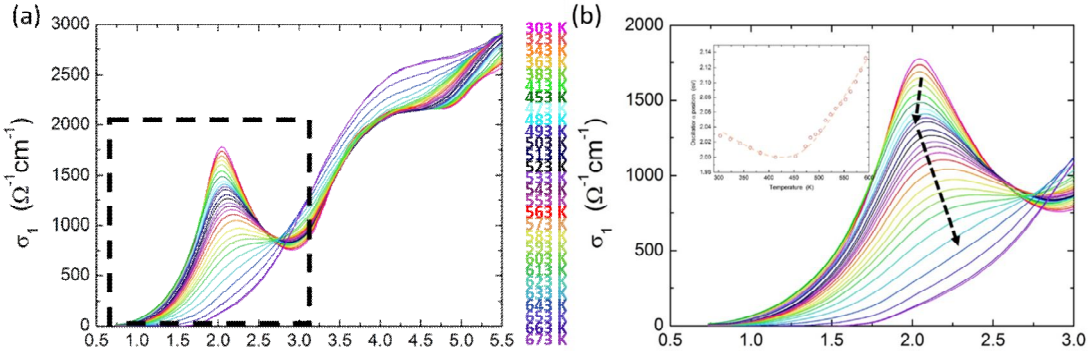

Figure 5. Real-time spectroscopic ellipsometry plot. (a) Optical conductivity as a function of photon energy. (b) Magnified view of Figure 5(a), (inset) Peak position based on Lorentz-Gaussian fitting.

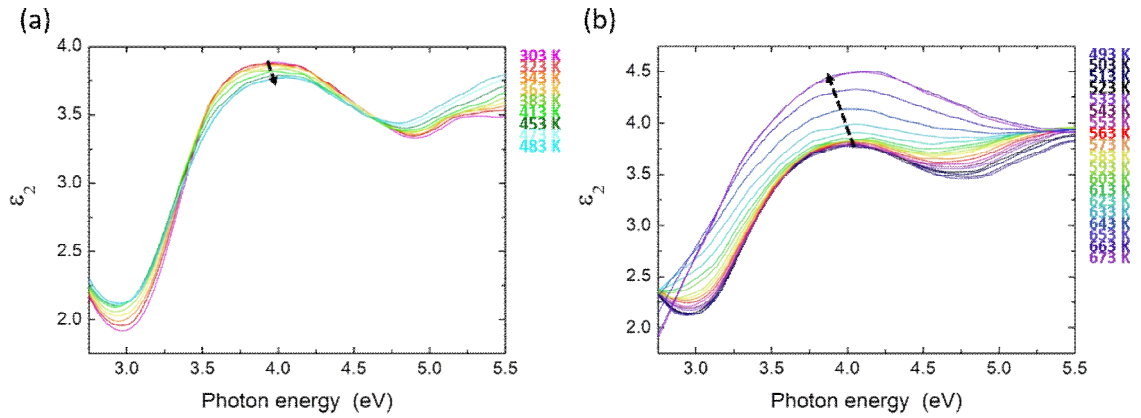

Figure 6. Dielectic function as a function of photon energy at (a) lower temperature range (303K ~ 483K), and (b) higher temperature range (493K ~ 673K).

For analysis of optical responses at higher photon energies the imaginary part of the dielectric constant (ε_2) is used, because the change is more visible in ϵ_2 than in σ_1. Now, focusing on the peak at around 4 eV, this feature also undergoes an anomaly at around 480K; at lower temperature the spectral weight is reduced, in constrast the peak gets predominant at higher temperature as shown in Figure 6 (a) and (b). The origin of this peak is still not clear, however current computational work in progress by our collaborator, C. Franchini *et al*, shows similar behavior, where peaks at higher temperature appear upon generating oxygen vacancies.

5.4 Discussion

In summary, based on the XRD and spectroscopic ellipsometry data, we confirmed that the CDW was suppressed upon generating oxygen vacancies by vacuum annealing, on the other hand, there was a mismatch between temperatures at which the suppression of the half-integer peak and of the gap induced by CDW happen. In other words, in XRD the lattice doubling totally vanished, but there is still the gap in the optical spectroscopy. This difference could be originated by the fact that XRD can probe only coherent long-range CDW ordering, on the other hand optical spectroscopy can measure averaged electronic structure from both long-range and realatively short-range ordering. As a result, we suggest that the long-range ordering is suppressed first by thermal flutuation, then short-range order is broken later by oxygen vacancies. This observation has considerable impact because it has been known that the optical gap is originated from long-range CDW ordering [3], while our work shows that the optical gap remains even when long-range ordering is destroyed.

In addition, thanks to the UHV annealing chamber equipped with real-time ellipsometer, we succesfully acquired the optical spectra of the $BaBiO_3$ doped with electrons by generating oxygen vacancies, which has been hindered by the fact that the $BaBiO_{3-x}$ reacts with carbons in the air producing amorphous compound. The optical spectrum of the oxygen vacant BBO showed two significant features. One is the reduced intensity of 2 eV peak due to the unbalanced ratio between Bi^{3+} and Bi^{5+}, which detroys the long-range ordering and forms pseudo-bipolarons. The other is the enhanced optical weight at higher photon energies ($3\ \mathrm{eV} < \mathrm{E} < 5\ \mathrm{eV}$) which needs further investigation.

For the exploration of the topological insulating phase in electron-doped BBO, more surface sensitive spectroscopic measurements are needed to confirm the characteristic Dirac cone shape in the surface band stucture.

References

[1] K. Foyevtsova, A. Khazraie, I. Elfimov, and G.A. Sawatzky, *Phys. Rev. B* **91**, 121114 (2015).

[2] R. A. Beyerlein, A. J. Jacobson and L. N. Yacullo, *Mat. Res. Bull* **20**, 877 (1985).

[3] S. Uchida, K. Kitazawa and S. Tanaka, *Phase transitions* **8**, 95 (1987).

Chapter 6

Conclusion

To summarize, the behavior of charge-density instability in $BaBiO_3$ thin films was studied utilizing its three dimensional character and the strong hybridization between bismuth and oxygen atoms [1]. By reducing thickness, the three-dimensional symmetry in the periodic lattice was suppressed such that the Bi atoms can feel the boundary of the material, therefore the CDW ordering was destroyed in the thin films thinner than critical thickness $d_c \sim 11$ unit cells. Similarly, the V_o spoiled the A_{1g} symmetry of oxygen octahedron simultaneously introducing extra electrons in the lattice, consequently the CDW ordering was broken in the oxygen deficient samples.

Altogether, we provide two important and clean tuning parameters that can manipulate the charge density wave in BBO without introducing chemical doping. Since this 3D-CDW is an insulating ground state for doped superconducting materials, these parameters could be utilized to study the relation between superconductivity and CDW, which has attracted much attention in copper oxide superconductors recently [2]. Furthermore, this electron-doped BBO could be the first step toward a materialization of topological insulator in oxide materials [3].

References

[1] K. Foyevtsova, A. Khazraie, I. Elfimov, and G.A. Sawatzky, *Phys. Rev. B* **91**, 121114 (2015).

[2] E H. da Silva Neto, *et al.*, *Science*. **343**, 393 (2014).

[3] Binghai Yan, Martin Jansen and Claudia Felser, *Nat. Phys*. **9**, 709 (2013).